THE JOURNAL OF PHYSICAL CHEMISTRY C

Article

pubs.acs.org/JPCC

Computational Model of Domain-Specific Reactivity on Coated Ferroelectric Photocatalysts

James J. Glickstein, Paul A. Salvador,* and Gregory S. Rohrer

Department of Materials Science and Engineering, Carnegie Mellon University, Pittsburgh, Pennsylvania 15213, United States

ABSTRACT: The optimization of coated ferroelectric photocatalysts represents a promising pathway toward competitive efficiencies. Here, we present a computational model that is used to predict the internal quantum efficiency (IQE) of individual coated ferroelectric domains. Criteria are identified that enable increased efficiencies. The net current favored on a negatively polarized domain of $BaTiO_3$ coated with a 20 nm TiO_2 (anatase) film is shown to be oxidation, whereas reduction is favored on positively polarized coated $BaTiO_3$ domains. The results indicate that the IQE of the minority carrier reaction (oxidation) at physical conditions reported in the literature is less than 1%. By increasing the carrier lifetime to approximately 100 ns, increasing the reduction reaction kinetics, and optimizing the potential, complementary electron and hole reactions of equal magnitude can occur separately on positive and negative domains with an IQE of over 90% (45% if operated in a Z-scheme). This analysis can be applied to heterostructured photocatalysts with various sources of charge-separating internal fields, including those that also absorb visible light, to ultimately maximize the solar to hydrogen efficiency.

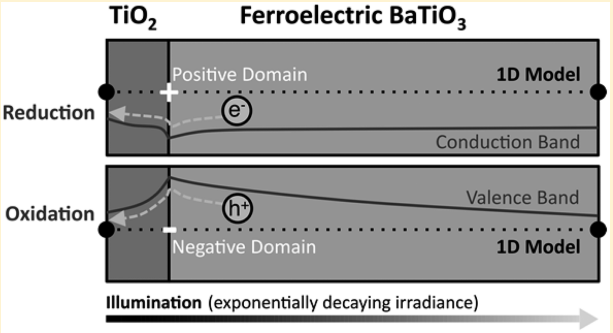

INTRODUCTION

The development of a particulate photocatalyst that can harvest solar energy to split water and efficiently produce hydrogen has the potential to revolutionize the energy industry.[1] However, limitations in efficiency relative to competing technologies have prevented commercialization.[2] Therefore, there has been a great deal of research into understanding what factors limit efficiencies[3] and to identify materials that exhibit improved efficiencies.[4]

One common issue is that the majority of water-splitting photocatalysts operate primarily as either a photoanode or a photocathode.[5] Efficiencies can be limited, therefore, by the balancing electrochemical reaction, by back-reactions of intermediates when the reactions are not separated, and by the recombination of minority carriers prior to their reaction.[6] Co-catalysts are commonly employed to mitigate these effects, as they promote the balancing half-reaction and allow overall water splitting to proceed.[7] However, cocatalysts are commonly precious metals that significantly increase cost and do not increase the performance to desired efficiencies. It is, therefore, of interest to investigate other mechanisms that promote balancing half-reactions and separate charge carriers within a photocatalyst.

Numerous studies have demonstrated that internal electric fields influence the reactivity of a material's surface.[8] Some materials have spatially varying near-surface internal fields that can drive electrons to one area of the surface and holes to another, thereby spatially separating the two water-splitting half-reactions on the surface of a single material (without a cocatalyst). One of the most common types of spatial selectivity arising from internal fields is the domain-selective reactivity observed in many ferroelectrics.[9] The empirical evidence for improved photocatalytic behavior in ferroelectrics is strong. The suggested origin of this behavior is that, by separating the location of surface reactions and separating the photogenerated charge carriers throughout the absorption depth, back-reactions and recombination are minimized.[10] Nevertheless, there have not been quantitative studies that describe the relative performance variation for different domains. In the current work, we focus on developing a computational model that captures the relevant charge carrier transport mechanisms in ferroelectric photocatalysts. We use this model to identify criteria that can be optimized to increase efficiencies to over 90%, indicating that there is significant room for improving catalysts by engineering the spatial variation of near-surface electric fields.

$BaTiO_3$ is one of the best-known ferroelectrics and is a well-studied photocatalyst.[11] The photoelectrochemical response of $BaTiO_3$ electrodes has been studied,[12] but not in a manner that can isolate the behavior of individual domains and reveal the precise effect of the polarization. Domain-selective reactivity on the surface of an illuminated ferroelectric (n-type) $BaTiO_3$ polycrystal submersed in aqueous $AgNO_3$ was demonstrated by Giocondi and Rohrer.[10,13] Solid Ag reduction reaction products were observed (using atomic force microscopy) in a pattern that coincided with the ferroelectric domain structure. The

Received: April 16, 2016
Revised: May 18, 2016
Published: May 23, 2016

DOI: 10.1021/acs.jpcc.6b03875
J. Phys. Chem. C 2016, 120, 12673−12684

Table 1. Summary of Material Parameters, Constants, and Variables Used in the Computations

Material Parameters					
description	symbol	film value	substrate value	unit	source
relative permittivity	ε_r	31	1200		26, 27
donor density	N_D	1×10^{18}	1×10^{18}	cm^{-3}	28, 29
acceptor density	N_A	1×10^{16}	1×10^{16}	cm^{-3}	
surface polarization magnitude	P	0	0, 26	$\mu C\ cm^{-2}$	30
electron mobility	μ_n	0.1	0.5	$cm^2\ V^{-1}\ s^{-1}$	29, 31
hole mobility	μ_p	2×10^{-3}	0.25	$cm^2\ V^{-1}\ s^{-1}$	32, 33
electron affinity	χ	4.2	4.2	eV	34, 35
band gap	E_g	3.2	3.2	eV	31, 36, 37
surface effective Richardson constant	$A^*_{n,p}$	1×10^7		$A\ m^{-2}\ K^{-2}$	38
conduction band effective density of states	N_c	7.9×10^{20}	5.5×10^{19}	cm^{-3}	40, 41[a]
valence band effective density of states	N_v	1.8×10^{19}	1.2×10^{20}	cm^{-3}	40, 41[a]
absorption coefficient	α	2×10^3	1×10^5	cm^{-1}	42−44
representative photon energy	E_{ph}	3.82	3.82	eV	
carrier recombination lifetime	τ_n, τ_p	1×10^{-9}	1×10^{-9}	s	45, 46

Constants			
description	symbol	value	unit
elementary charge	q	1.602×10^{-19}	C
vacuum permittivity	ε_0	8.854×10^{-12}	$F\ m^{-1}$
temperature	T	298	K
Boltzmann constant	k	1.381×10^{-23}	$J\ K^{-1}$
incident irradiance	I_0	1×10^4	$W\ m^{-2}$
metal work function	ϕ_m	4.76	eV

Variables					
description	symbol	unit	description	symbol	unit
Schottky barrier height	ϕ_B	V	carrier current densities	J_n, J_p	$A\ m^{-2}$
depth	x	m	carrier generation rate	$G_{n,p}$	$m^{-3}\ s^{-1}$
electric field	E	$V\ m^{-1}$	carrier recombination rate	$U_{n,p}$	$m^{-3}\ s^{-1}$
electrostatic potential	ϕ	V	conduction band energy	E_c	eV
carrier densities	n, p	m^{-3}	valence band energy	E_v	eV

[a]Calculated from effective masses.

complementary domains were shown to support oxidation reactions that formed solid Pb products when submersed in an aqueous lead acetate solution.[13] It was shown through these marker reactions that domains of positive polarizations promoted reduction and domains of negative polarizations promoted oxidation.

Despite the promising demonstration of domain-specific reactivity on the surface of $BaTiO_3$, Ba leaching has been shown to dissolve the material over time in aqueous solution.[14−16] When $BaTiO_3$ is coated with a 10 nm thin film of chemically stable TiO_2, the film exhibits spatially selective reactivity that correlates with the domain structure of the $BaTiO_3$ substrate in a fashion identical to that of the bare substrate reactivity.[17−19] Given the low absorption coefficient of the film, it was proposed that carriers photogenerated in the substrate ($BaTiO_3$) were driven by internal fields associated with the domain polarization to the substrate/film interface and then traversed the film (TiO_2) to react at the surface. As the film thickness was increased to 30 nm, the influence of the underlying substrate polarization on the spatial reactivity also decreased, and domain-specific reactivity was no longer apparent when the film was beyond 50 nm thick.[18] Also, the reactivity of both the $TiO_2/BaTiO_3$ heterostructures and the bare $BaTiO_3$ substrate were not shown to vary significantly with the crystal orientation or phase of TiO_2, indicating that the direction of the polarization was most important, not the magnitude of the polarization resolved into the direction of the surface normal. Li et al.[20] showed that hierarchically structured photocatalysts could be designed that incorporated high surface area nanocrystalline TiO_2 shells on microcrystalline $BaTiO_3$ cores. These catalysts had improved performance relative to their components, illustrating further the potential of using heterostructured ferroelectric photocatalysts.

It should be noted that recent work has demonstrated similar spatially selective behavior for visible light absorbing ferroelectric substrates[21] and their heterostructures.[22] Spatially selective reactivity has also been observed due to different sources of internal electric fields, including polar surface terminations, phase boundaries, and polymorph junctions.[8] These versatile mechanisms for producing spatially selective reactivity represent a promising approach to achieving highly efficient photocatalysts. However, the methods used to characterize their performance have been primarily qualitative.

Quantitatively evaluating the efficiency and understanding how to optimize the performance is essential for future photocatalyst design. However, it is often difficult to control independently all of the variables in the laboratory. Reported computational efforts have focused primarily on modeling the solution/photocatalyst interface.[23] However, modeling the transport of carriers throughout the depth of the photocatalyst is essential to understanding the influence of buried charges.

In this work, we have developed a quantitative computational model of the heterostructured ferroelectric photocatalysts, using a general model that represents any potential buried

DOI: 10.1021/acs.jpcc.6b03875
J. Phys. Chem. C 2016, 120, 12673−12684

charge separation mechanism. Simulations are then used to assess the impact of specific parameters in the underlying physical model on reactivity and to develop directions to improve catalyst performance. TiO_2 (anatase)/$BaTiO_3$ heterostructures were simulated to make direct comparisons with the thorough photochemical results available in the literature. Simulations of films of varying thicknesses over a range of applied voltages on domains of different types were carried out, and the results expand upon insights gained from the physical experiments in the literature. The results provide a framework for predicting and optimizing the physical performance of these heterostructures. Specifically to these heterostructures, we show that, by increasing the carrier lifetime to approximately 100 ns, increasing the reduction reaction (majority carrier) kinetics, and optimizing the potential (externally or through pH), complementary electron and hole reactions of equal magnitude can occur separately on positive and negative domains with an internal quantum efficiency (IQE) of over 90% (45% if operated in a Z-scheme). The model is extensively described in the next section (Theoretical Methods). Collections of different simulations are subdivided in the Results, focusing separately on the nature of band bending and light absorption, film thickness effects, current−voltage behaviors, the effects of different model parameters, and the optimal efficiency.

THEORETICAL METHODS

Simulations were designed and conducted using the commercial finite element software package COMSOL Multiphysics.[24] The semiconductor physics incorporated into the model are similar to those recently reported by Garcia-Esparza and Takanabe.[25] Using the built-in semiconductor module, a fully coupled damped Newton method was employed to simultaneously solve Poisson's equation (see Table 1 for variable definitions)

$$\nabla\cdot E = -\nabla^2\phi = \frac{q}{\varepsilon_0\varepsilon_r}(p - n + N_D - N_A + P) \tag{1}$$

the electron and hole current continuity equations

$$\frac{\partial n}{\partial t} = \frac{1}{q}\nabla\cdot J_n + G_n - U_n \tag{2a}$$

and

$$\frac{\partial p}{\partial t} = -\frac{1}{q}\nabla\cdot J_p + G_p - U_p \tag{2b}$$

and the electron and hole drift and diffusion equations

$$J_n = q(\mu_n nE + \mu_n kT\nabla n) \tag{3a}$$

and

$$J_n = q(\mu_n nE + \mu_n kT\nabla n) \tag{3b}$$

The key parameters and variables used in the model are summarized in Table 1. Equations 1, 2a, 2b, 3a, and 3b were used to calculate the electrostatic potential (ϕ) and carrier (electron and hole) concentrations (n and p) throughout the heterostructure. Dopant concentrations, recombination losses, photogeneration rates, and various material parameters were all factored into the computations. Whenever values were selected, they were taken from the literature with an aim to describe previously reported marker reaction results.

A one-dimensional (1D) geometry was used, as shown in Figure 1. The geometry was discretized into thousands of mesh

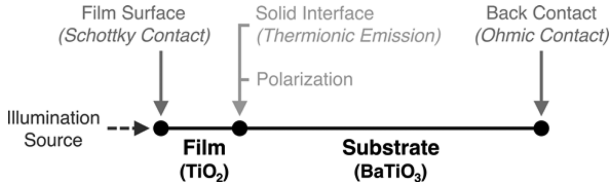

Figure 1. Heterostructure model geometry and corresponding physics.

elements that are most narrowly defined near the film surface, throughout the thin film, and at the solid interface between the film and substrate. Uniform n-type doping (N_D) was applied throughout the film and substrate, with a relatively smaller concentration of p-type counterdopants also included (N_A). The ferroelectric polarization (P) was modeled in the form of a sheet charge density at the node representing the film/substrate interface and was locally incorporated into Poisson's equation (eq 1). An Ohmic contact fixed the substrate Fermi level at the back contact node.

The arrival of charge carriers to the film surface (where reaction can occur) is dependent on the electrostatic potential (band bending) and the relative photogeneration and recombination rates. The conduction (E_C) and valence (E_V) band energies were defined (relative to the reference level) throughout the heterostructure by determining the spatially varying electrostatic potential (ϕ), and combining it with the fixed electron affinity (χ) and band gap (E_g) of the material, as follows:

$$E_c = -q(\Phi + X) \tag{4a}$$

and

$$E_v = -q(\Phi + X + E_g) \tag{4b}$$

Illumination was modeled as being incident at the film surface and penetrating through the film and into the substrate. The photogeneration rate ($G_{n,p}$), which was applied equally to electrons and holes, was derived from the Beer−Lambert law:

$$G_{n,p} = \frac{I_0\alpha}{E_{ph}}e^{-\alpha x} \tag{5}$$

The irradiance (I_0) of photons with sufficient energy to be absorbed by TiO_2 and $BaTiO_3$ was estimated from marker reaction setups described in the literature.[17−19] Considering the spectrum of the illumination source used in the literature, a representative photon energy (E_{ph}) was selected to approximate the total irradiance as originating from a monochromatic source.

Photogenerated carriers drift and diffuse throughout the heterostructure until either being collected at the film surface or recombining internally. The method of recombination used in the model was trap-assisted Shockley−Read−Hall (SRH) recombination. The SRH recombination rate ($U_{n,p}$), defined as

$$U_{n,p} = \frac{np - N_cN_ve^{-E_g/kT}}{\tau_p(n + \sqrt{N_cN_v}e^{-E_g/2kT}) + \tau_n(p + \sqrt{N_cN_v}e^{-E_g/2kT})} \tag{6}$$

depends strongly on the local carrier concentrations (n and p) and the carrier lifetimes ($\tau_{n,p}$).

The surface of the thin film coating in contact with solution was modeled as a Schottky contact, with thermionic emission governing the electron and hole currents at the surface:

DOI: 10.1021/acs.jpcc.6b03875
J. Phys. Chem. C 2016, 120, 12673−12684

Table 2. Summary of Key Variable Inputs for the Film (f) and Substrate (s)[a]

Figure	film thickness (nm)	$A^{*}_{n}{}^{f}$ (A m^{-2} K^{-2})	$A^{*}_{p}{}^{f}$ (A m^{-2} K^{-2})	P^{s} (μC cm^{-2})	V_a (V vs SCE)	$\tau_{n,p}{}^{f,s}$ (s)
2	20	1×10^{7}	1×10^{7}	0, ±26	−0.3	1×10^{-9}
3	variable	1×10^{7}	1×10^{7}	0, ±26	−0.3	1×10^{-9}
4	variable	1×10^{1}	1×10^{1}	0, ±26	−0.3	1×10^{-9}
5a,b	20	variable	variable	±26	variable	1×10^{-9}
6a	20	1×10^{1}	1×10^{1}	±26	variable	variable
6b	variable	1×10^{1}	1×10^{1}	±26	−0.3	variable
7a	20	1×10^{7}	1×10^{1}	±26	variable	1×10^{-7}
7b	variable	1×10^{7}	1×10^{1}	±26	variable	1×10^{-7}

[a]The voltage, V_a, is applied at the back contact (see Figure 1).

$$J_n = -\frac{A^{*}_{n} T^2}{N_c}(n - N_c e^{-\Phi_B/kT}) \tag{7a}$$

and

$$J_p = \frac{A^{*}_{p} T^2}{N_v}(p - N_v e^{-(E_g-\Phi_B)/kT}) \tag{7b}$$

The work function of the metal (ϕ_m) in the Schottky contact was defined as the approximate electrochemical potential of the solution being modeled, calculated here to be 4.76 eV. The Schottky barrier height (ϕ_B) was determined self-consistently in the model, and is a function of the electrochemical potential of electrons in the metal ("solution") and semiconductor, the polarization at the film/substrate interface, and the (applied) potential at the back Ohmic contact.

Ultimately, we are most interested in the currents through the Schottky contact, as this represents the injection of carriers into the reactive solution (modeled as a metal Schottky contact). The currents reported herein, accordingly, were measured at the surface of the semiconducting film. The value of the leading coefficient in eqs 7a and 7b, known as the effective Richardson constant, A^*, can greatly affect the measured surface currents. The constant is commonly calculated as follows:[47]

$$A^* = \lambda\frac{4\pi q m_e k^2}{h^3} \tag{8}$$

wherein the leading coefficient, λ, is a material-specific parameter (dependent on the charge carrier effective mass) that is typically determined empirically. The transport of carriers across the film/substrate interface was similarly modeled with thermionic emission, with the potential barriers defined by the interfacial band bending after equilibration of the film and substrate Fermi levels. The Richardson constants for each material were calculated using eq 8 with λ equated to the charge carrier effective mass (computed from the effective density of states) of TiO_2 and $BaTiO_3$.

In the application of this model to photocatalysis at a solution interface, A^* acts as a kinetic parameter influencing the rate at which arriving carriers react with species in solution (producing faradic current in the model). Therefore, it can be treated as a variable parameter used as a general measure of reaction kinetics and was adjusted to explore different operating regimes and to model surfaces of different relative reactivities (given the same number of available carriers). For instance, a sufficiently high A^* value models the regime where the rate of delivery of charge carriers to the surface limits the reaction rates, whereas a sufficiently low A^* value models the regime where slow reaction rates limit the surface current. We consider the upper limit of A^* as the value for the material when in contact with a metal, which can be calculated using eq 8 to be 1×10^7 A m^{-2} K^{-2}.[38,39] Replacing the metal with an electrolyte generally decreases A^*, as the value becomes directly proportional to the reaction rate constant and the concentration of redox species in solution.[48] The reported height of marker reaction deposits in a set period of time can be used to estimate the currents required to produce them.[17−19] This current magnitude was compared to simulated current outputs and the A^* value adjusted until the simulation output matched the estimated physical currents. The A^* value that produces current magnitudes on the order of those estimated from the literature is 1×10^1 A m^{-2} K^{-2}, significantly lower than the theoretical maximum value. These two values for A^*, corresponding to the theoretical upper limit and the estimation from physical results in the literature, are referred to in the Results as high and low A^*, respectively.

The focus of the model is to determine the percentage of photogenerated carriers created throughout the heterostructure that are able to navigate through the spatially varying electrostatic potential and ultimately generate surface current before recombining. The ratio of photogenerated carriers to the reacted carriers (the number passing through the Schottky contact or film surface) can be quantified and used to determine the internal quantum efficiency (IQE). The maximum photogenerated current (representing an IQE of 100%), wherein all photogenerated carriers are transferred to the film surface, is 262 mA cm^{-2} (using the irradiance approximating reported marker reactions). The setup of the model is directly comparable to that of a photoelectrochemical potentiostat-controlled testing environment (commonly employed in the literature), wherein faradic current is a function of the applied voltage. Voltages were applied to the heterostructure by shifting the potential of the Ohmic back contact (V_a) without adjusting the Schottky contact at the film surface.

Unlike in photoelectrochemical testing, there is no back contact in typical marker reaction characterization. Therefore, the results, while providing novel insight into the photoelectrochemical behavior of these heterostructures, must only subjectively be compared to reported marker reaction results. The slower of the two (oxidation and reduction) half-reactions limits the overall reaction rate (and the rate of the other half-reaction) in a marker reaction setup. Additionally, the voltage is not externally controlled, and the reactions occur at the open-circuit voltage under illumination (V_{OC}*). An estimation of V_{OC}* (again approximating the photochemical tests reported in the literature) is input into the model as an applied potential to simulate the marker reaction conditions. The V_{OC} without illumination is taken as the metal ("solution") work function of 4.76 eV, which is 0.016 V vs a saturated calomel electrode

DOI: 10.1021/acs.jpcc.6b03875
J. Phys. Chem. C 2016, 120, 12673−12684

(SCE). Given the material parameters in Table 1, the flat-band potential (E_{fb}) can be computed to be approximately −0.34 V vs SCE for bulk TiO_2. With increasing illumination, the potential increases from the dark (no illumination) V_{OC} and approaches E_{fb}. Given the very high level of illumination, we have approximated V_{OC}* as being near but slightly positive of E_{fb} at a value of −0.3 V vs SCE.

RESULTS

A series of computational experiments were performed with the goals of revealing the effects of substrate polarizations on the current output of the $TiO_2/BaTiO_3$ heterostructure and understanding how various material parameters influence these results. Table 2 summarizes the values of key parameters that were varied to produce the main figures. For clarity, we have subdivided the Results as follows. The first section presents a description of the band bending and light absorption in the heterostructure. The second section considers the effect of the film thickness on the current through the heterostructure. The third section describes the potential dependence of the current and identifies the applied potential for the maximum internal quantum efficiency. The fourth section considers the influence of the carrier lifetime, the magnitude of the polarization, and the Richardson constant. The final section describes the characteristics of a heterostructure optimized for efficiency.

Band Bending and Light Absorption. The effects of neutral (P_0), positive (P_+), and negative (P_-) polarizations at the film/substrate interface on simulated energy level diagrams are shown in Figure 2 for a 20 nm film. The voltage at the back

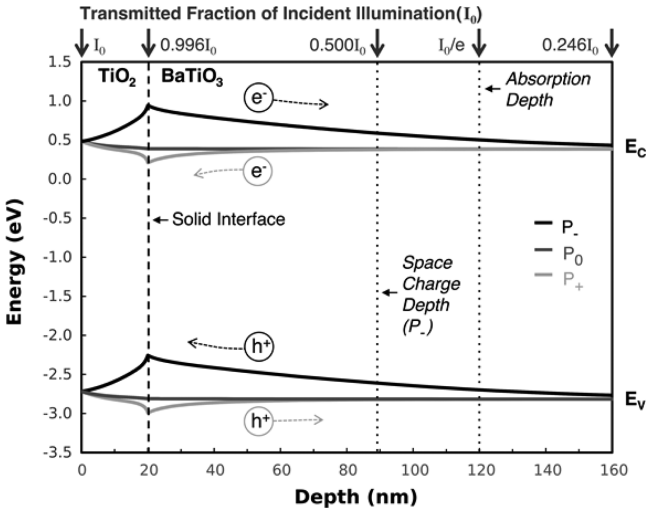

Figure 2. Simulated energy level diagrams of heterostructured anatase TiO_2 (20 nm) films on $BaTiO_3$ substrates for neutral, negative, and positive substrate polarizations implemented at the solid interface. The directions of electron (e^-) and hole (h^+) drift currents are shown. A simulated light source is incident on the surface of the film, with the majority of photogeneration occurring in the substrate and ∼75% of incident light absorbed within the depth shown.

contact was set to −0.3 V vs SCE, the estimated illuminated V_{OC} (V_{OC}*). For a neutral polarization (no charge at the interface), there is slight upward band bending at the surface of the film that arises from the Schottky barrier. The film cannot completely screen this charge, and the band bending penetrates into the substrate. A positive polarization (P_+ = +26 μC cm^{-2}) at the film/substrate interface lowers the conduction and valence bands at the solid interface, resulting in downward band bending in the substrate and increased upward band bending in the film approaching the surface. As such, holes photogenerated in the substrate are driven away from the solid interface, while electrons are driven toward it. Conversely, a negative polarization (P_- = −26 μC cm^{-2}) raises the bands at the solid interface, resulting in significant upward band bending in the substrate and generating a deep space charge layer and strong downward band bending throughout the 20 nm anatase film. The nature of the substrate band bending for negative polarizations favors hole transport in the substrate toward the solid interface and electron transport to the bulk (away from the interface). These simulated results are similar to the qualitative schematics used to interpret the prior observations.[18]

The simulated irradiance is incident on the film surface, on the left edge of Figure 2. Due to the low absorption coefficient of anatase, 99.6% of incident photons are transmitted to the substrate, where the vast majority of photogeneration occurs. It is therefore crucial that carriers photogenerated in this substrate region are separated to avoid recombination. Roughly 75% of the illumination is absorbed within the first 140 nm of the substrate, with a fraction of e^{-1} of the incident illumination transmitted beyond 100 nm into the substrate (representing the absorption depth). For the negative polarization, the potential value dropped by band bending from the solid interface to the bulk substrate value reaches a fraction of e^{-1} at a depth of 89 nm (representing the space charge depth). Roughly 50% of the incident illumination has been absorbed within the space charge depth (though the bands remain bent further into the solid where more absorption occurs). The total simulated thickness of the substrate is 1 μm, to allow sufficient depth for all incident illumination to be absorbed. Only the first 140 nm of the substrate is displayed in Figure 2, with the back Ohmic contact being applied at a depth of 1020 nm into the heterostructure (for a 20 nm film).

For a neutral polarization, the slight upward band bending favors hole transport to the surface. However, the driving electric field is only minimally present at the absorption depth. On the other hand, the field is much stronger at the absorption depth for negative polarizations, leading to an increased percentage of holes being photogenerated in a region where a field drives them toward the surface. Similarly, electrons are expected to accumulate at the solid interface for positive polarizations more so than for neutral polarizations as a result of the substrate band bending. When holes accumulate at the solid interface for negative polarizations and electrons accumulate for positive polarizations, the band bending in the film provides a barrier (in both cases) to charge transfer to the surface (no tunneling was included in the model). To investigate the net effect of the electric fields introduced by positive and negative polarizations, the surface currents must be examined.

Effect of Film thickness on Current Density. Figure 3 shows the electron and hole currents at the film surface for different polarizations and varying film thicknesses. The open circles represent (positive) hole current densities, and the closed circles mark (negative) electron current densities. The value of the kinetic parameter, A*, was set to its maximum value, which is sufficiently high to not meaningfully limit the surface currents. The potential was set to the estimated illuminated open-circuit condition (−0.3 V vs SCE). The hole

DOI: 10.1021/acs.jpcc.6b03875
J. Phys. Chem. C 2016, 120, 12673−12684

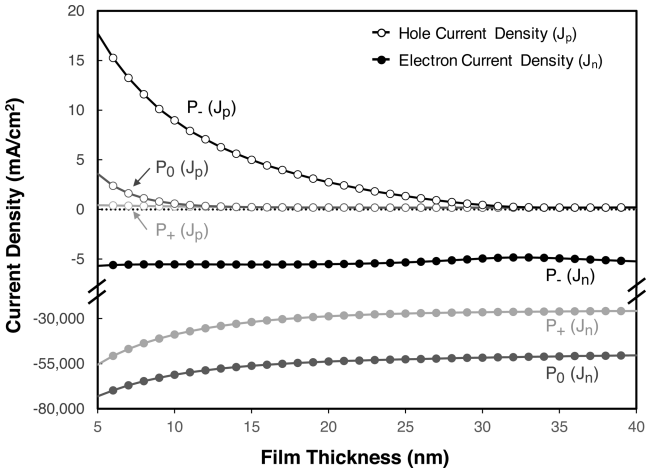

Figure 3. Simulated TiO_2 (anatase)/$BaTiO_3$ film thickness dependence of surface electron and hole currents (high A^* value) for neutral, negative, and positive substrate polarizations.

currents, or minority carrier currents, are entirely photogenerated and behave as expected from the above discussion. At the 20 nm film thickness used to generate the energy level diagrams shown in Figure 2, the negative polarization has the highest hole current magnitude, at 17.7 mA cm^{-2}. The neutral and positive polarizations have much smaller hole currents (respectively 3.59 and 0.421 mA cm^{-2}). The deeper and stronger electric field shuttling holes to the solid interface for negative polarizations results in a significantly higher hole current compared to that for neutral (and positive) polarizations. This is true despite the unfavorable downward band bending introduced in the 20 nm film.

The behavior of the electron currents is slightly different. The electron current, which is the majority carrier current, is largely not photogenerated but driven by the applied voltage in the simulation. In other words, similar values are observed with or without illumination. The neutral domain has a slightly higher magnitude (-7.31×10^4 mA cm^{-2}) than the positive domain (-5.55×10^4 mA cm^{-2}), owing to the upward band bending throughout the 20 nm film (both are much larger than the maximum photogenerated current of 262 mA cm^{-2}). However, the electron current density for negative polarizations is minimal, being only −5.69 mA cm^{-2}, resulting from the large barrier at the solid interface. Quantitatively, the negative polarization at the film/substrate interface decreases the majority carrier current by 3−4 orders (which remains true for all film thicknesses). Thus, for a negative domain (at this applied voltage), the minority and majority carrier current densities are of similar magnitudes.

Examining the thickness dependence of the currents in Figure 3 reveals that hole currents are highest for thinner films (results for films below 5 nm are not included because of the diminished applicability of the underlying physics and the probable increased significance of tunneling effects for such thin films). Below film thicknesses of 30 nm, the hole current for negative polarization domains increases as the film thickness decreases. For thicknesses greater than 30 nm, the hole current is independent of the thickness and is fixed to a small value. Because nearly all of the photogeneration occurred in the substrate (for all of these thicknesses), these results indicate that fewer and fewer holes traverse the film barrier without recombining as the thickness increases.

The high A^* value used in Figure 3 represents the regime in which reaction rates at the film surface do not significantly limit the current (high A^*). As discussed in the Theoretical Methods, we estimated that an A^* value of 1×10^1 A m^{-2} K^{-2} produced currents similar to the marker reaction rates. The thickness dependence of the electron and hole currents for different polarizations with the low A^* value is displayed in Figure 4. Again, the potential was set to −0.3 V vs SCE. Similar

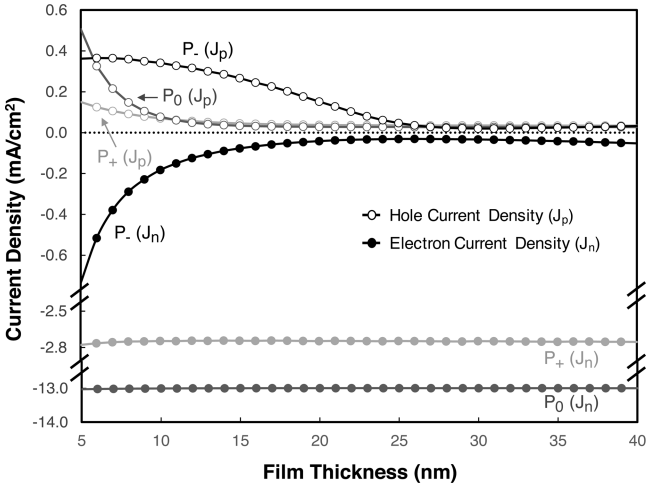

Figure 4. Simulated TiO_2 (anatase)/$BaTiO_3$ film thickness dependence of electron and hole current densities (low A^* value) for neutral, negative, and positive substrate polarizations.

to Figure 3, the current contribution of photogenerated holes originating in the substrate disappears beyond roughly 30 nm film thickness. In contrast to Figure 3, however, the highest value of the hole current is observed for the 5 nm film with a neutral polarization. Nevertheless, for films thicker than 5 nm, the hole current is highest for the negative polarization (similar to Figure 3). The electron current magnitude is again highest for the neutral polarization and lowest for the negative polarization. Overall, the current densities in Figure 4 (low A^*) are much smaller than those in Figure 3 (high A^*). The hole currents are 1−2 orders of magnitude lower, while the electron currents are 3−4 orders of magnitude lower. In fact, the highest electron current magnitudes in Figure 4 are now comparable to those for holes. The electron current is penalized more so than the hole current in the low A^* case because of the applied bias (it is slightly anodic of the flat-band condition for a neutral polarization).

As the film thickness increases beyond the 40 nm displayed in Figures 3 and 4, the current densities retain approximately the same values as they become reflective of photogeneration in the film. It should be noted that the current densities do not approach the same values regardless of polarization as a consequence of the boundary conditions of the model. The voltage of the modeled Schottky contact is fixed; therefore, when a large polarization is introduced at the solid interface, the degree of band bending at the surface of even the thickest films varies with the sign and magnitude of the buried polarization charge. These effects are not as noticeable for films less than approximately 40 nm thick (the displayed domain of Figures 3 and 4) when the energy bands in the film are bent throughout the entire thickness.

Variation of the Current with the Applied Potential and Potential for Maximum Efficiency. Several current−

DOI: 10.1021/acs.jpcc.6b03875
J. Phys. Chem. C 2016, 120, 12673−12684

voltage curves are depicted in Figure 5a for a 20 nm thick film. Only the electron currents (solid symbols) for positive

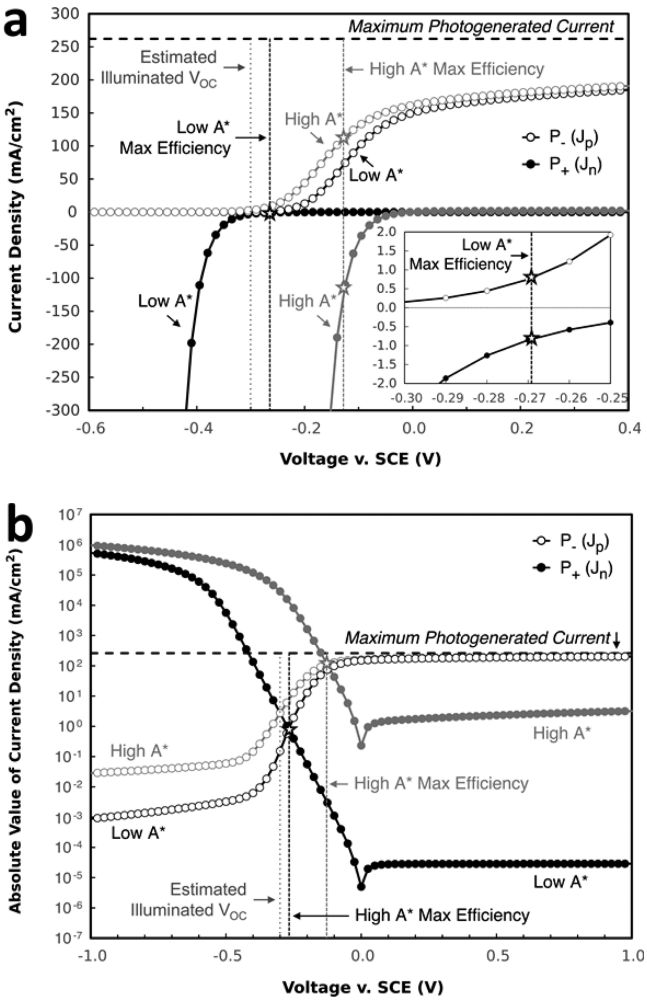

Figure 5. Simulated voltage dependence of electron (J_n) and hole (J_p) current densities at the surface of a 20 nm TiO_2 film on $BaTiO_3$, displayed in (a) linear and (b) semilog representations. Conducted separately for both high (theoretical maximum) and low (corresponding to reported physical results) A^* values. The voltage, assumed to be the open-circuit potential under illumination (V_{OC}^*), is noted along with the potentials that maximize the IQE for each A^* value (with the low A^* region of interest expanded in the inset of (a)).

polarizations and hole current (open symbols) for negative polarizations are shown, since these are the most relevant when considering domain-specific reactivity. The current−voltage output for both the high A^* (lighter symbols) and low A^* (darker symbols) cases are included in Figure 5. The maximum photogenerated current for this illumination is marked as a horizontal line (at 262 mA cm^{-2}). The band structure for this film at V_{OC}^* (marked with a vertical line in Figure 5) is shown in Figure 2 (and the current values at this voltage are given in Figures 3 and 4). From Figure 2, it is clear that the $J-V$ behavior of the Schottky contact will be a strong function of the domain orientation, as the band diagrams are significantly different. Specifically, the buried charge for the polar domains perturbs the band bending at the Schottky contact, which should lead to significantly different turn-on voltages (V_{on}) in the $J-V$ curves. As will be demonstrated below, these shifts in V_{on} for the different domains open a window of operation to achieve large efficiencies in ferroelectric photocatalysts.

The minority carrier photogenerated hole currents shown in Figure 5a are described as follows. The photogenerated hole currents onset at V_{on}^+, increase smoothly with more anodic (positive) voltages, and saturate at a current near 190 mA cm^{-2}, which represents an IQE of over 70%. At cathodic voltages, more negative than V_{on}^+ for the negative domains, the hole currents are approximately zero for both A^* values. The difference between the two curves for the different A^* values is small, with the higher A^* material having higher current values at lower anodic voltages above V_{on}^+ (i.e., the curve is shifted slightly to the left).

The majority carrier electron currents (which are not generally photogenerated in the model) are described as follows. For large anodic voltages, more positive than the turn-on voltage (V_{on}^-) for positive domains, the electron currents are approximately zero. In the high A^* case, the electron current rapidly increases in magnitude for voltages more cathodic than V_{on}^-. Note that there is no saturation in the majority carrier current, and it quickly becomes larger than the maximum photogenerated current in the model. On the linear scale for the low A^* case, the general shape of the electron current is the same as that for the high A^* case, but it appears that the onset potential (V_{on}^-) is shifted to a significantly more cathodic voltage compared to the high A^* electron current. If the $J-V$ behavior is plotted on a semilog plot as in Figure 5b, the low and high A^* electron currents onset at virtually the same potential, but the rate of increasing current magnitude is greatly reduced for low A^*, and the electron current appears to onset at a more cathodic potential on a linear plot. Note that the downward band bending in the substrate at V_{OC}^* (for P_+ in Figure 2) favors emission of electrons from the substrate into the film, while the film band bending presents a barrier to their emission into the solution: i.e., the electron population at the film/substrate interface is high. A large A^* value permits a significant fraction of the majority carriers emitted from the substrate to pass through as faradic current, while a low A^* value prevents most of these carriers from registering as faradic current through the film surface (though there is a smaller leakage component). By moving to more cathodic voltages, the band bending in the film ultimately favors emission into the solution and the current rapidly increases, despite the low A^* value.

At any given voltage, the performance of the photocatalyst will be limited by the slower of the two reactions (i.e., the domain with the lower of the two current values). If we assume that positive and negative domains producing electron and hole faradic currents (respectively) operate at the same potential, then the voltage at which the performance of the heterostructure is maximized will be at the potential for which the equal magnitudes of the electron and hole currents are maximized. These potentials of maximum efficiency for the low and high A^* values are labeled in Figure 5. The corresponding maximum balanced electron and hole current magnitudes are found where the dashed lines intersect the current−voltage curves, and can be used to compute the IQE_{max}. In either case, hole currents limit the overall current for voltages left of the dashed maximum efficiency line, while electrons limit the current for voltages to the right.

For the 1D simulations presented here, the maximum efficiency represents the balanced performance for electrons in positively polarized domains and holes in negatively polarized

DOI: 10.1021/acs.jpcc.6b03875
J. Phys. Chem. C 2016, 120, 12673−12684

Table 3. Summary of Conditions That Optimize Performance for Different Multiples of the $BaTiO_3$ Substrate Polarization Magnitude (P_{BTO} = 26 μC cm^{-2}) Buried beneath a 20 nm TiO_2 Film[a]

		0	$0.25P_{BTO}$	$0.5P_{BTO}$	P_{BTO}	$2P_{BTO}$
A^*_n low, A^*_p low, τ = 10^{-9} s (shown in Figure 5 for P_{BTO})	V (V vs SCE)	−0.161	−0.206	−0.230	−0.269	−0.339
	J (mA cm^{-2})	0.0582	0.277	0.479	0.807	1.53
	IQE_{max} (%)	0.022	0.11	0.18	0.31	0.58
A^*_n high, A^*_p high, τ = 10^{-9} s (shown in Figure 5 for P_{BTO})	V (V vs SCE)	0.026	−0.080	−0.096	−0.126	−0.184
	J (mA cm^{-2})	0.478	74.5	96.2	113	131
	IQE_{max} (%)	0.18	28	37	43	50
A^*_n high, A^*_p low, τ = 10^{-7} s (shown in Figure 7 for P_{BTO})	V (V vs SCE)	−0.071	−0.111	−0.121	−0.147	−0.201
	J (mA cm^{-2})	60.6	236	240	242	245
	IQE_{max} (%)	23	90	92	92	94

[a]Optimal performance is represented by the voltage at which the electron current density for positive polarizations is equal in magnitude to the hole current density for negative polarizations. The maximum efficiencies (without considering any lost efficiency from the applied voltage) and the voltage at which they are achieved are displayed for the low A^* value, the high A^* value, and an increased carrier lifetime (with high A^*_n and low A^*_p; see Figure 7).

domains. However, it is unknown what charge transfer may occur at the boundaries between neighboring, oppositely polarized domains in a 2D (or 3D) geometry. If the charge carriers not dominant in the surface reactions recombine at the domain boundaries, then the efficiency limit ($IQE_{Z,max}$) would be half of the IQE_{max}, as the Z-scheme photocatalyst loses half of all photogenerated carriers. However, if the nondominant carriers drift across the domain boundaries to oppositely polarized domains and are driven to the surface to react, then the IQE_{max} value represents the highest theoretical efficiency. Therefore, the theoretically achievable efficiency predicted by this 1D model is somewhere between IQE_{max} and $0.5(IQE_{max})$ (=$IQE_{Z,max}$), depending on the extent of charge transfer at domain boundaries.

Influence of the Richardson Constant, Polarization, and Carrier Lifetime on Efficiency. When A^* is not significantly limiting (high A^*), the IQE_{max} for balancing oxidation and reduction reactions separated to oppositely polarized domains is 43%, which occurs at V_a = −0.13 V (SCE). This voltage that maximizes performance is shifted away from V_{OC}* = −0.3 V (SCE) by +0.17 V, the equivalent of 2−3 pH units in solution and only 14% of the 1.23 V water-splitting voltage. Considering the fractional voltage input (relative to the water-splitting voltage) to represent a fractional energy loss, the voltage efficiency would still be 37% (or 19% for the Z-scheme). By operating at this optimal voltage, the IQE for high A^* is increased nearly 40-fold relative to the IQE = 1.1% at V_{OC}*. The IQE_{max} when A^* is at the value estimated from reported marker reaction data (low A^*) is only 0.31%, occurring at V_a = −0.27 V (SCE), or +0.03 V from V_{OC}*. This value is roughly 5 times higher than that at V_{OC}* (IQE = 0.063%) for the low A^* case. Note that the steep drop in optimal performance from the high to low A^* values indicates that slow kinetics of the majority carrier reaction limits the optimal performance of the real photocatalyst to only a fraction of the possible value. Examination of Figure 5 reveals that the reduced kinetics for the majority carriers suppresses the current in the voltage region just below V_{on}^- (≈ 0 V in Figure 5b), causing the electron current to further limit the reactivity to the cathodic side of V_{on}^-. The low A^* electron current is only slightly greater than the hole current at V_{OC} *. On the other hand, faster majority carrier kinetics at the surface (high A^*) results in large electron currents in the voltage region just below V_{on}^-, which opens up a wide voltage region to the anodic side of V_{on}^+ in which the hole current limits the reaction but increases with increasing positive voltages.

The optimal operating potentials and corresponding currents (and IQE) are shown in Table 3 for various polarization magnitudes to assess the degree to which ferroelectrics enhance photocatalytic performance. For neutral domains (zero polarization), the optimal performance is reduced by 2 orders of magnitude for a high A^* and 1 order of magnitude for low A^* from that for domains with the $BaTiO_3$ polarization (P_{BTO}). For domains with only one-fourth of P_{BTO}, there is still a significant increase in optimal efficiency compared to that for zero polarization, and only a relatively small drop from the performance of P_{BTO}. The relatively small differences between the IQE_{max} for $-0.25P_{BTO}$ (28% for high A^*) and $2P_{BTO}$ (50% for high A^*) is consistent with findings in the literature that similar reactivity effects are observed for differently oriented grains, for different materials (that have different spontaneous polarization magnitudes), and for different sources of internal fields (or surface charges).[8]

Because the primary mechanism for lost efficiency in the minority carrier current is carrier recombination, the carrier lifetime (τ) value should be addressed relative to performance. In the prior simulations, a τ of 10^{-9} s was used, as this is a value often reported in the literature. Figure 6a shows the current−voltage behavior for a 20 nm film using the low A^* value (poor surface kinetics) and values of τ = 10^{-9}, 10^{-7}, and 10^{-5} s. For the minority carrier current, increasing the lifetime from 10^{-9} s shifts the apparent onset (V_{on}^+) to significantly more cathodic values, increases the saturation current values significantly to more than 90% of the maximum value, and shifts the voltage at which saturation is achieved to more cathodic values. All of these changes open the window further for improved efficiencies. For the majority carrier current, the changing lifetime does not meaningfully affect the electron current, which exhibits a relatively cathodic onset in the linear plot due to the low A^* value (see Figure 5b). As a result, the kinetically limited electron currents in Figure 6a limit the achievable efficiencies for almost all carrier lifetimes. For such photocatalysts, performance improvement will be achievable by modifying the surface kinetics (A^*), as described previously.

The thickness dependencies of the hole current density for negative ($P_-(J_p)$) and positive ($P_+(J_p)$) polarizations are shown in Figure 6b for three carrier lifetimes. Increasing the lifetime increases both the negative and positive polarization hole currents. However, the negative polarization domains still

DOI: 10.1021/acs.jpcc.6b03875
J. Phys. Chem. C 2016, 120, 12673−12684

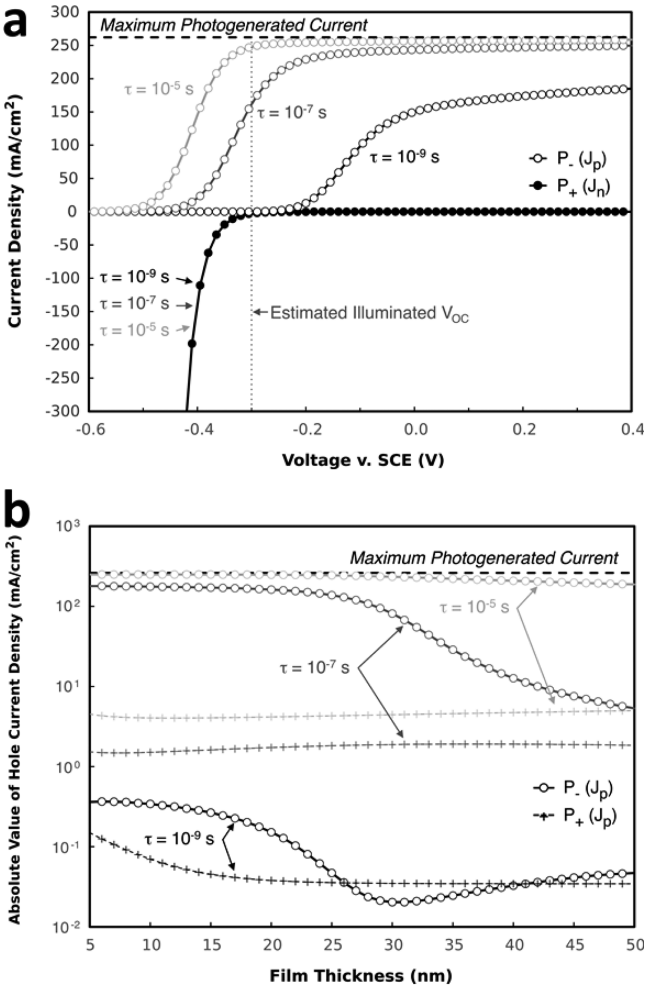

Figure 6. (a) Simulated voltage dependence of electron (J_n) and hole (J_p) current densities (low A^* value) at the surface of a 20 nm TiO_2 (anatase) film on $BaTiO_3$ for various values of the carrier recombination lifetime (τ). (b) Simulated TiO_2 (anatase)/$BaTiO_3$ film thickness dependence of hole current densities (low A^* value) produced by negative and positive substrate polarizations for various values of the carrier recombination lifetime (τ).

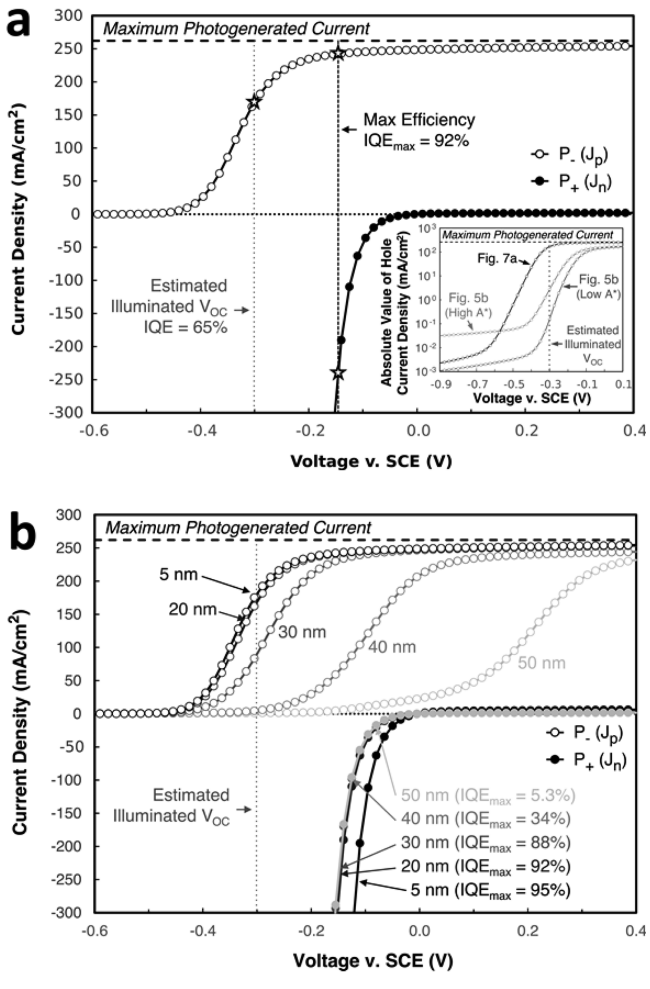

Figure 7. Simulated voltage dependence of electron (J_n) and hole (J_p) current densities ($A^*_n = 1 \times 10^7$ A m^{-2} K^{-2}, $A^*_p = 1 \times 10^1$ A m^{-2} K^{-2}) for $\tau = 10^{-7}$ s for $BaTiO_3$ coated with (a) a 20 nm TiO_2 (anatase) film and (b) various TiO_2 (anatase) film thicknesses (the arrows labeling the electron currents indicate the voltage at which the IQE is maximized). The inset in (a) shows the semilog $J-V$ characteristic of the minority carrier current for a 20 nm film compared to those from Figure 5.

exhibit significantly higher hole currents relative to the positive polarization domains. Increasing the hole carrier lifetime also extends the film thickness range over which the minority carriers photogenerated in the substrate contribute significantly to the surface current.

Optimized Heterostructures. Figure 5 indicates that the maximum efficiency is limited in the high A^* case because the hole current onset is too anodic. Figure 6a indicates that the maximum efficiency is limited in the greater carrier lifetime case because the electron current onset is too cathodic. Combined, these figures indicate that a near-optimal device can be obtained in a ferroelectric (which minimizes the internal recombination in the substrate) with a high lifetime for the minority carriers and fast surface kinetics for the majority carriers. This is borne out by simulations, as shown in Figure 7a, which displays the simulated current–voltage output using a lifetime on the order of 10^{-7} s and a high A^*_n value for electrons (but a low A^*_p value for holes) for a 20 nm film. The IQE at the estimated illuminated V_{OC} is 65%, and the maximum efficiency jumps to 92% (at $V_a = -0.146$ V (SCE)). Considering the small shift from open circuit (0.154 V), the voltage efficiency is still 81% for this heterostructure. The inset of Figure 7a reveals that increasing the lifetime fundamentally shifts the minority carrier current onset to more cathodic potentials. Increasing the lifetime further (to 10^{-5} s), increasing A^*_p, or decreasing the film thickness would result in reducing the losses even further. The efficiency can be increased slightly by increasing the substrate polarization magnitude (see Table 3), but the IQE_{max} is still 90% even when only one-fourth of the $BaTiO_3$ polarization is applied.

The thickness dependence of the current–voltage curve and the corresponding maximum efficiencies are displayed in Figure 7b. The arrows labeling the electron current density curves mark the voltage at which the electron and hole currents become equal (and IQE_{max} is achieved). There is only a small increase in performance when the film thickness is decreased to 5 nm (IQE_{max} = 95%), with the increase primarily resulting from a small anodic shift in the majority carrier current. The minimal thickness dependence of the hole current between 5 and 20 nm is evident from Figure 6b for the 10^{-7} s lifetime. Beyond a 30 nm film thickness in Figure 7b, the achievable IQE quickly drops off before reaching only 5.3% for a 50 nm film.

DOI: 10.1021/acs.jpcc.6b03875
J. Phys. Chem. C 2016, 120, 12673–12684

Even for the 50 nm film, the hole current eventually saturates near the maximum theoretical value, but does so at a voltage well anodic of the electron current onset.

DISCUSSION

The predominant result from the marker reactions in the literature was that, for TiO_2 (anatase)/$BaTiO_3$ heterostructures (and other similar materials), reduction reactions were more active on coated positive domains and oxidation reactions were more active on negative domains. It is evident from Figure 2 that negative and positive polarizations generate band bending in the substrate that favors increased hole and electron transport to the solid interface, respectively, compared to a neutral polarization. However, it is also evident that the band bending in the film impedes the transfer of these carriers that accumulate at the interface from reaching the surface and contributing to the current. The net effects of the favorable band bending in the substrate and the unfavorable band bending created in the film are evident in the currents in Figure 3 as a function of the thickness. Below a thickness of approximately 30 nm, the band bending effects in the film are overwhelmed by those in the substrate, similar to that observed in the literature.[18]

The simulations demonstrate that negative polarizations produce the highest magnitude hole current and the lowest magnitude electron current, which supports the qualitative explanation for domain-specific reactivity.[18] They also suggest that physical observations can be explained using only the basic assumptions about carrier excitation and transport incorporated into the computational model. In other words, tunneling through energy barriers or polarization-dependent surface potentials need not be implemented to produce the physical observations. This outcome does not change when the kinetics are more limiting, as in Figure 4. The simulations also imply that the net effect of a polarized substrate with multiple domains may increase the efficiency of the overall reaction (compared to an unpolarized substrate).

Another important insight from Figures 3 and 4 is that, for a minimally absorbing anatase film, thinner films result in increased hole current, with hole transfer from the substrate being largely absent for films thicker than 30 nm. Published marker reaction results revealed that domain-specific reactivity was clearly visible in atomic force microscopy (AFM) for a 10 nm film, less so for a 30 nm film, and not clearly discernible for a 50 nm film.[18] This finding is generally consistent with the computational result that the current contribution of holes photogenerated in the substrate is minimal beyond 30 nm. Therefore, in designing a TiO_2 (anatase)/$BaTiO_3$ photocatalyst, the film should be as thin as possible to also maintain chemical stability.

A primary goal of building a computational model of coated ferroelectric photocatalytic materials was to quantitatively estimate the performance and understand how the performance could be optimized. Figure 5 reveals that controlling the potential is crucial to achieving the optimal overall reaction rate. It is evident from Table 3 that, when the optimal potential is used, the performance is at least 1 order of magnitude higher for a polarized substrate than for an unpolarized one. To calibrate the model so that it mimicked the physical situation, values of the reactivity parameter (A^*) were assumed to reproduce the reported results. Using this relatively low A^* value, the IQE at V_{OC}^* is only 0.063%, which increases to an IQE_{max} of 0.31% when the potential is adjusted.

To achieve the much more desirable IQE_{max} of 43% for the high A^* value, the kinetics must be fast enough to approach the behavior of a Schottky metal contact to TiO_2. In particular, it is the effect of A^*_n on the majority carrier current onset that enables such a high increase in IQE_{max}, because the majority carrier onset voltage on positive domains becomes increasingly anodic with increased surface kinetics (A^*). However, it is clear that A^* is a surface parameter, and therefore has a much more significant effect on the majority carrier than it does on the minority carrier (which is not necessarily present in high concentrations near the surface). To increase the efficiency beyond 43%, the minority carrier recombination lifetime should be increased. In the simulations, this was achieved by increasing τ by 2 orders of magnitude from the 1 ns obtained from the literature.[45] There is a wide range of carrier lifetimes reported in the literature for TiO_2 and $BaTiO_3$ depending on the growth conditions and processing. A lifetime increased by 2 orders of magnitude by reducing the density of recombination sites results in a sharper and more cathodic hole current onset, as shown in Figure 6a. When combined with faster electron kinetics in Figure 7, the IQE_{max} is increased to 92% for a 20 nm film and 95% for a 5 nm film. These numbers were found at voltages slightly shifted from the open-circuit condition, but even accounting for the lost energy owing to the applied voltage (and for the Z-scheme nature of the two domain reactions), the efficiencies are still in the range of 80% (or 40% for Z-scheme).

This same modeling approach can be extended to a 2D geometry to incorporate the influence of charge transfer between neighboring domains. It can also ultimately be applied to optimizing the performance of visible light absorbing substrates with internal fields with the goal of developing a photocatalyst with an economically competitive solar to hydrogen efficiency.

CONCLUSIONS

A 1D computational model was designed in COMSOL to predict the photocatalytic performance (IQE) of TiO_2 films on ferroelectric $BaTiO_3$, and criteria were identified that enable increased efficiencies. Assumptions of classical semiconductor device behavior and a Schottky contact at the surface were sufficient to produce domain-specific electron and hole current densities that generally support reported physical results. The predicted domain specificity was not significantly altered when the polarization magnitude was varied. The estimated internal quantum efficiencies of the heterostructures (previously characterized only qualitatively) are below 1%. By increasing the carrier lifetime, increasing the reduction reaction kinetics, and optimizing the potential all within physically reasonable ranges, complementary electron and hole reactions of equal magnitude can occur separately on positive and negative domains with an IQE of over 90% (45% if operated in a Z-scheme).

AUTHOR INFORMATION

Corresponding Author

*E-mail: paul7@andrew.cmu.edu. Phone: 412-268-2702.

Notes

The authors declare no competing financial interest.

DOI: 10.1021/acs.jpcc.6b03875
J. Phys. Chem. C 2016, 120, 12673−12684

■ ACKNOWLEDGMENTS

We acknowledge the support of National Science Foundation Grant DMR 1206656.

■ REFERENCES

(1) Pinaud, B. A.; Benck, J. D.; Seitz, L. C.; Forman, A. J.; Chen, Z.; Deutsch, T. G.; James, B. D.; Baum, K. N.; Baum, G. N.; Ardo, S.; et al. Technical and Economic Feasibility of Centralized Facilities for Solar Hydrogen Production via Photocatalysis and Photoelectrochemistry. *Energy Environ. Sci.* **2013**, *6*, 1983−2002.

(2) Office of Energy Efficiency & Renewable Energy, U.S. Department of Energy. Multi-Year Research, Development, and Demonstration Plan: 2015 Production Section, 2015. http://energy.gov/sites/prod/files/2015/06/f23/fcto_myrdd_production.pdf, (accessed March 21, 2016).

(3) Li, J.; Wu, N. Semiconductor-Based Photocatalysts and Photoelectrochemical Cells for Solar Fuel Generation: a Review. *Catal. Sci. Technol.* **2015**, *5*, 1360−1384.

(4) Ismail, A. A.; Bahnemann, D. W. Photochemical Splitting of Water for Hydrogen Production by Photocatalysis: a Review. *Sol. Energy Mater. Sol. Cells* **2014**, *128*, 85−101.

(5) Morrison, S. R. *Electrochemistry at Semiconductor and Oxidized Metal Electrodes*; Plenum Press: New York, 1980.

(6) Bard, A. J. Photoelectrochemistry and Heterogeneous Photocatalysis at Semiconductors. *J. Photochem.* **1979**, *10*, 59−75.

(7) Yang, J.; Wang, D.; Han, H.; Li, C. Roles of Cocatalysts in Photocatalysis and Photoelectrocatalysis. *Acc. Chem. Res.* **2013**, *46*, 1900−1909.

(8) Li, L.; Salvador, P. A.; Rohrer, G. S. Photocatalysts with Internal Electric Fields. *Nanoscale* **2014**, *6*, 24−42.

(9) Tiwari, D.; Dunn, S. Photochemistry on a Polarisable Semi-Conductor: What do We Understand Today? *J. Mater. Sci.* **2009**, *44*, 5063−5079.

(10) Giocondi, J. L.; Rohrer, G. S. Spatially Selective Photochemical Reduction of Silver on the Surface of Ferroelectric Barium Titanate. *Chem. Mater.* **2001**, *13*, 241−242.

(11) Rajeshwar, K.; Singh, P.; Dubow, J. Energy Conversion in Photoelectrochemical Systems − a Review. *Electrochim. Acta* **1978**, *23*, 1117−1144.

(12) Nasby, R. D.; Quinn, R. K. Photoassisted Electrolysis of Water using a $BaTiO_3$ Electrode. *Mater. Res. Bull.* **1976**, *11*, 985−992.

(13) Giocondi, J. L.; Rohrer, G. S. Spatial Separation of Photochemical Oxidation and Reduction Reactions on the Surface of Ferroelectric $BaTiO_3$. *J. Phys. Chem. B* **2001**, *105*, 8275−8277.

(14) Nesbitt, H. W.; Bancroft, G. M.; Fyfe, W. S.; Karkhanis, S. N.; Nishijima, A.; Shin, S. Thermodynamic Stability and Kinetics of Perovskite Dissolution. *Nature* **1981**, *289*, 358−362.

(15) Neubrand, A.; Lindner, R.; Hoffmann, P. Room-Temperature Solubility Behavior of Barium Titanate in Aqueous Media. *J. Am. Ceram. Soc.* **2000**, *83*, 860−864.

(16) Adair, J. H.; Crampo, J.; Mandanas, M. M.; Suvaci, E. The Role of Material Chemistry in Processing $BaTiO_3$ in Aqueous Suspensions. *J. Am. Ceram. Soc.* **2006**, *89*, 1853−1860.

(17) Burbure, N. V.; Salvador, P. A.; Rohrer, G. S. Influence of Dipolar Fields on the Photochemical Reactivity of Thin Titania Films on $BaTiO_3$ Substrates. *J. Am. Ceram. Soc.* **2006**, *89*, 2943−2945.

(18) Burbure, N. V.; Salvador, P. A.; Rohrer, G. S. Photochemical Reactivity of Titania Films on $BaTiO_3$ Substrates: Origin of Spatial Selectivity. *Chem. Mater.* **2010**, *22*, 5823−5830.

(19) Burbure, N. V.; Salvador, P. A.; Rohrer, G. S. Photochemical Reactivity of Titania Films on $BaTiO_3$ Substrates: Influence of Titania Phase and Orientation. *Chem. Mater.* **2010**, *22*, 5831−5837.

(20) Li, L.; Rohrer, G. S.; Salvador, P. A. Heterostructured Ceramic Powders for Photocatalytic Hydrogen Production: Nanostructured TiO_2 Shells Surrounding Microcrystalline $(Ba,Sr)TiO_3$ Cores. *J. Am. Ceram. Soc.* **2012**, *95*, 1414−1420.

(21) Schultz, A. M.; Zhang, Y.; Salvador, P. A.; Rohrer, G. S. Effect of Crystal and Domain Orientation on the Visible-Light Photochemical Reduction of Ag on $BiFeO_3$. *ACS Appl. Mater. Interfaces* **2011**, *3*, 1562−1567.

(22) Zhang, Y.; Schultz, A. M.; Salvador, P. A.; Rohrer, G. S. Spatially Selective Visible Light Photocatalytic Activity of $TiO_2/BiFeO_3$ Heterostructures. *J. Mater. Chem.* **2011**, *21*, 4168−4174.

(23) Bai, S.; Jiang, J.; Zhang, Q.; Xiong, Y. Steering Charge Kinetics in Photocatalysis: Intersection of Materials Syntheses, Characterization Techniques and Theoretical Simulations. *Chem. Soc. Rev.* **2015**, *44*, 2893−2939.

(24) COMSOL Multiphysics, version 5.1, COMSOL AB, Stockholm, Sweden, www.comsol.com.

(25) Garcia-Esparza, A. T.; Takanabe, K. A Simplified Theoretical Guideline for Overall Water Splitting using Photocatalyst Particles. *J. Mater. Chem. A* **2016**, *4*, 2894−2908.

(26) Euken, A.; Buchner, U. A. Die Dielecrizitatskonstante schwach polare Kristalle and ihre Temperaturabhangigkeit. *Z. Phys. Chem. B* **1934**, *27*, 321.

(27) Roberts, S. Dielectric Constants and Polarizabilities of Ions in Simple Crystals and Barium Titanate. *Phys. Rev.* **1949**, *76*, 1215−1220.

(28) Breckenridge, R. G.; Hosler, W. R. Electrical Properties of Titanium Dioxide Semiconductors. *Phys. Rev.* **1953**, *91*, 793−802.

(29) Berglund, C. N.; Baer, W. S. Electron Transport in Single-Domain, Ferroelectric Barium Titanate. *Phys. Rev.* **1967**, *157*, 358−366.

(30) Lines, M. E.; Glass, A. M. *Principles and Applications of Ferroelectrics and Related Materials*; Clarendon: Oxford, U.K., 1970.

(31) Tang, H.; Prasad, K.; Sanjinès, R.; Schmid, P. E.; Lévy, F. Electrical and Optical Properties of TiO_2 Anatase Thin Films. *J. Appl. Phys.* **1994**, *75*, 2042−2047.

(32) Deskins, N. A.; Dupuis, M. Intrinsic Hole Migration Rates in TiO_2 from Density Functional Theory. *J. Phys. Chem. C* **2009**, *113*, 346−358.

(33) Günter, P.; Jean-Pierre, H. *Photorefractive Materials and Their Applications I: Fundamental Phenomena*; Topics in Applied Physics; Springer-Verlag: Berlin, 1988.

(34) Xiong, Y.; Lu, X. *Metallic Nanostructures*; Springer: Cham, Switzerland, 2015.

(35) Kung, H. H.; Jarrett, H. S.; Sleight, A. W.; Ferretti, A. Semiconducting Oxide Anodes in Photoassisted Electrolysis of Water. *J. Appl. Phys.* **1977**, *48*, 2463−2469.

(36) Wemple, S. H. Polarization Fluctuations and the Optical-Absorption Edge in $BaTiO_3$. *Phys. Rev. B* **1970**, *2*, 2679−2689.

(37) Hafid, L.; Godefroy, G.; El Idrissi, A.; Michel-Calendini, F. Absorption Spectrum in the Near U.V. and Electronic Structure of Pure Barium Titanate. *Solid State Commun.* **1988**, *66*, 841−845.

(38) Szydlo, N.; Poirier, R. I-V and C-V Characteristics of Au/TiO2 Schottky Diodes. *J. Appl. Phys.* **1980**, *51*, 3310−3312.

(39) Tang, J.; White, M.; Stucky, G. D.; McFarland, E. W. Electrochemical Fabrication of Large-Area Au/TiO_2 Junctions. *Electrochem. Commun.* **2003**, *5*, 497−501.

(40) Enright, B.; Fitzmaurice, D. Spectroscopic Determination of Electron and Hole Effective Masses in a Nanocrystalline Semiconductor Film. *J. Phys. Chem.* **1996**, *100*, 1027−1035.

(41) Erhart, P.; Albe, K. Thermodynamics of Mono and Di-Vacancies in Barium Titanate. *J. Appl. Phys.* **2007**, *102*, 084111.

(42) Sekiya, T.; Ichimura, K.; Igarashi, M.; Kurita, S. Absorption Spectra of Anatase TiO_2 Single Crystals Heat-Treated under Oxygen Atmosphere. *J. Phys. Chem. Solids* **2000**, *61*, 1237−1242.

(43) Tang, H.; Lévy, F.; Berger, H.; Schmid, P. E. Urbach Tail of Anatase TiO_2. *Phys. Rev. B: Condens. Matter Mater. Phys.* **1995**, *52*, 7771−7774.

(44) Bäuerle, D.; Braun, W.; Saile, V.; Sprüssel, G.; Koch, E. E. Vacuum Ultraviolet Reflectivity and Band Structure of $SrTiO_3$ and $BaTiO_3$. *Z. Phys. B: Condens. Matter Quanta* **1978**, *29*, 179−184.

(45) Ozawa, K.; Emori, M.; Yamamoto, S.; Yukawa, R.; Yamamoto, S.; Hobara, R.; Fujikawa, K.; Sakama, H.; Matsuda, I. Electron-Hole Recombination Time at TiO_2 Single-Crystal Surfaces: Influence of Surface Band Bending. *J. Phys. Chem. Lett.* **2014**, *5*, 1953−1957.

DOI: 10.1021/acs.jpcc.6b03875
J. Phys. Chem. C 2016, 120, 12673−12684

(46) Brost, G. A.; Motes, R. A.; Rotge, J. R. Intensity-Dependent Absorption and Photorefractive Effects in Barium Titanate. *J. Opt. Soc. Am. B* **1988**, *5*, 1879−1885.
(47) Crowell, C. R. The Richardson Constant for Thermionic Emission in Schottky Barrier Diodes. *Solid-State Electron.* **1965**, *8*, 395−399.
(48) Pelizzetti, E., Schiavello, M., Eds. *Photochemical Conversion and Storage of Solar Energy*; Kluwer Academic Publishers: Palermo, Italy, 1991; pp 193−212.

DOI: 10.1021/acs.jpcc.6b03875
J. Phys. Chem. C 2016, 120, 12673−12684